BEST AVAILABLE IMAGES

Defective images within this document are accurate representations of the original documents submitted by the applicant.

Defects in the images may include (but are not limited to):

- BLACK BORDERS
- TEXT CUT OFF AT TOP, BOTTOM OR SIDES
- FADED TEXT
- ILLEGIBLE TEXT
- SKEWED/SLANTED IMAGES
- COLORED PHOTOS
- BLACK OR VERY BLACK AND WHITE DARK PHOTOS
- GRAY SCALE DOCUMENTS

IMAGES ARE BEST AVAILABLE COPY.

As rescanning documents *will not* correct images, please do not report the images to the Image Problem Mailbox.

Measurement of Interstitial Convective Heat Transfer and Frictional Drag for Flow Across Metal Foams

J.-J. Hwang
Mem. ASME
e-mail: jjhwang@chu.edu.tw
Department of Mechanical Engineering,
Chung-Hua University,
Hsinchu, Taiwan 300, ROC

G.-J. Hwang
Fellow ASME

R.-H. Yeh

Department of Power Mechanical Engineering,
National Tsing Hua University,
Hsinchu, Taiwan 300, ROC

C.-H. Chao
Department of Electrical Engineering,
Ta-Hwa Institute of Technology,
Hsinchu, Taiwan 300, ROC

Convective heat transfer and friction drag in a duct inserted with aluminum foams have been studied experimentally. The combined effects of foam porosity (ε=0.7, 0.8, and 0.95) and flow Reynolds number ($1900 \leq Re \leq 7800$) are examined. Frictional drags for flow across the aluminum foam are measured by pressure taps, while interstitial heat transfer coefficients in the aluminum foam are determined using a transient single-blow technique with a thermal non-equilibrium two-equation model. Solid material temperature distribution is further measured for double check of the heat transfer results. To understand the frictional drag mechanisms, smoke-wire flow visualization is conducted in the aluminum-foam ducts. Results show that both the friction factor and the volumetric heat transfer coefficient increase with decreasing the foam porosity at a fixed Reynolds number. In addition, the aluminum foam of ε=0.8 has the best thermal performance under the same pumping power constraint among the three aluminum foams investigated. Finally, empirical correlations for pore Nusselt number are developed in terms of pore Reynolds number under various foam porosities. [DOI: 10.1115/1.1416690]

Keywords: Convection, Heat Transfer, Inverse, Non-Equilibrium, Porous Media

Introduction

Porous media have been widely used in industrial applications such as electronic cooling, thermal energy absorber, geothermal system and many others. They can be in the form of packed beds, sintered materials, or foam materials. In the past, a large amount of research works for packed beds and sintered materials has been done [1–10], and extensive data and empirical correlations for convective heat transfer coefficient and friction factor are available now, which cover a large range of particle diameters, Reynolds numbers and fluids. The heat transfer and friction in porous foam materials, however, has not been studied to the same extent as that of pack beds and sintered materials [11–14]. Thus, the related data and correlations are relatively sparse. It is inappropriate to use the data or correlations of packed beds and sintered materials to predict the convective heat transfer inside foam materials because their internal structures are quite different [13]. In addition, the porosity of foam materials (ε>0.7) is much larger than the porosity of the packed beds or sintered materials (ε <0.476) [15]. Therefore, substantial data about the fluid flow and heat transfer characteristics inside foam materials are required to develop and optimize the design of such advanced devices.

Two kinds of heat transfer coefficients are often employed to depict heat transfer characteristics in porous media for their own application purpose, i.e., wall heat transfer coefficient and interstitial heat transfer coefficient. The first one always illustrates the global extent of heat transfer augmentation from the wall surface where the porous medium attaches. These surface heat transfer data are useful in the design of heat sinks such as electronics cooling [8,10,11,16]. The second one describes the heat exchange between the fluid stream and the solid matrix of the porous medium. Technologic applications of these data include thermal energy absorbers, advanced burners or incinerators, compact heat exchangers, etc. [7,12,13,17]. The present paper focuses on the interstitial heat transfer characteristics of the aluminum foams. Several relevant studies related to the interstitial heat transfer characteristics in porous media are briefly reviewed below. Golombok et al. [17] employed the heat regenerator technique to measure the heat transfer coefficient between the flowing gas and the metal fiber of a burner. The porosity of the porous fibrous material was fixed at ε=0.8. Results showed that the heat transfer coefficient for laminar flows increased rapidly with increasing gas flow. Vafai and Sozen [6] analyzed the thermal-fluid characteristics for flow through a packed bed of spherical particles of a fixed porosity ε=0.39. They used the fluid-to-solid heat transfer coefficients from an empirical correlation established by Gamson et al. [18]. Results showed that the local thermal equilibrium condition was very sensitive to the particle Reynolds number and the Darcy number. Younis and Viskanta [12] utilized a single-blow method to determine the volumetric heat transfer coefficients between the air stream and ceramic foam under a small range of the porosity ($0.83 \leq \varepsilon \leq 0.87$). It was found that the volumetric heat transfer coefficients were significantly different from previous data for packed beds and sintered metals. Ichimiya [13] evaluated the convective heat transfer between the fluid and the solid material of an aluminum-ceramic foam (ε=0.87) by comparing the measured and predicted Nusselt number on the heated wall of a porous channel. In his prediction, the analysis was performed under the assumption that porous media was constructed by small spherical particles.

It is evident that the above studies related to the interstitial heat transfer in porous media were performed under a fixed porosity or a small range of porosity. Strictly speaking, the results concerning the effect of porosity on the interstitial heat transfer and friction of metal foam have not been reported yet. Therefore, the objective of this paper is to investigate the combined effects of porosity (ε =0.7, 0.8 and 0.95) of the aluminum foam and the flow Reynolds number ($1900 \leq Re \leq 7800$) on interstitial heat transfer and friction characteristics in an aluminum-foam channel. Several issues are discussed in the present paper. First, experiments are conducted to examine the effect of porosity on the pressure-drop for flow across the aluminum foam, which has not been studied before. To quali-

Contributed by the Heat Transfer Division for publication in the JOURNAL OF HEAT TRANSFER. Manuscript received by the Heat Transfer Division November 17, 2000; revision received May 15, 2001. Associate Editor: D. Poulikakos.

tatively understand the frictional drag mechanism in the channel inserted with different-porosity aluminum foams, flow visualization using a smoke-wire technique is undertaken. Then, the volumetric heat transfer coefficient between the gas and the aluminum foam is obtained by using a transient single-blow technique. It is hard to directly measure the interstitial heat transfer coefficient of the porous medium because of the difficulty in the measurement of the temperature difference between the gas and solid phases. Therefore, an inverse method of transient single-blow technique is used to determine the convective heat transfer coefficients between the fluid and solid phases of the aluminum foams. Subsequently, by quoting the friction and heat transfer data, a comparison of the thermal performance among the three aluminum foams is made under two constraints, i.e., constant pumping power and constant though flow rate. Finally, empirical correlations for pore Nusselt numbers are developed in terms of pore Reynolds number for the different-porosity aluminum foam, which may be helpful in the design of related devices such as compact heat exchanger and thermal energy absorber. In addition, the interstitial heat transfer and friction data presented can provide a reference of computational-fluid-dynamic-based studies relating the heat transfer in the foam materials.

Experimental Program

Apparatus. An experimental setup for the measurement of interstitial heat transfer characteristic in the aluminum foam is shown in Fig. 1. It consists of an airflow circuit, the test section, and instruments. Air from a 2 hp compressor first enters into a surge tank for the supply of airflow in the circuit. The compressed air released from the surge tank passes through two filters and a refrigeration dehydrator to remove oil, water and particulate material. It then flows into a settling chamber to reduce the possible noise and to attain a uniform axial velocity profile. Before entering the test section, airflow is heated by passing through a specially designed plate heater, which is formed by 30-μm thick stainless steel foil wound around in a bakelite frame. The hot air then traverses the aluminum-foam test section, and finally exits from the test section to the outside of the building via an exhaust system. A digital flow meter is situated at the downstream of the test section to measure the volumetric flow rate through the test section. The test channel as shown in Fig. 2 made of Plexiglas® plates has a rectangular cross section of 60×25.4 mm^2. The aluminum foam of size $60\times25.4\times60$ mm^3 is cut in the way that the sides are flush with the channel walls for a good contact. The aluminum foam is fitted into the channel, and subsequently the entire test section is bolted tightly from outside. Two pressure taps located at the inlet and the outlet of the test section measure the

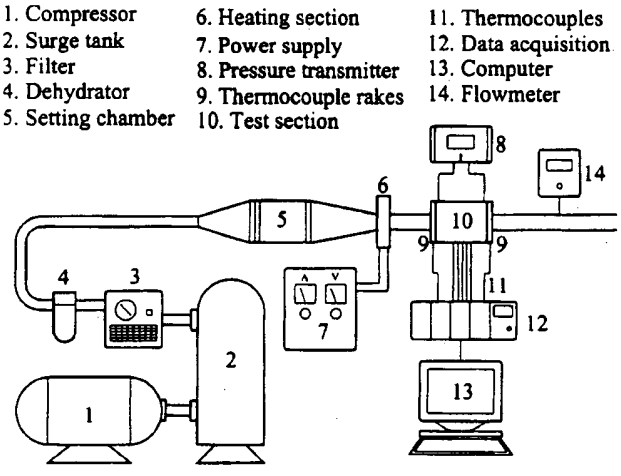

Fig. 1 Sketch of the experimental setup

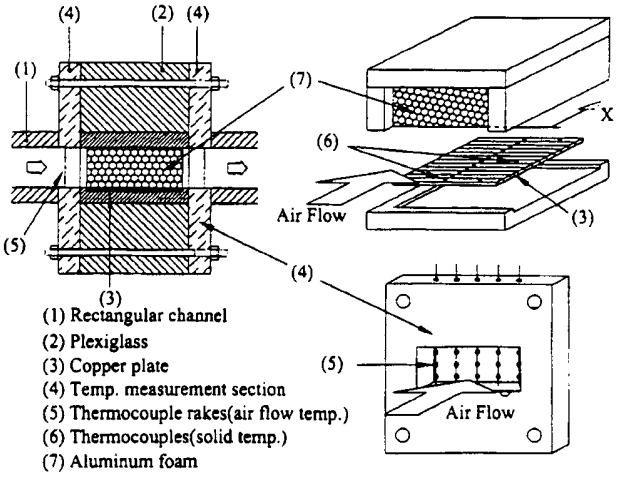

Fig. 2 Schematic drawing of the test section

static pressure differences across the test sample. They are connected to a micro-differential transmitter to display the pressure signals. At both the upstream and the downstream of the test section, five thermocouple rakes (each with three beads) are used to measure the averaged airflow temperature. The transient responses of temperature signals are transferred and subsequently recorded by a real-time hybrid recorder (YOKOGAWA DA100) with a sample rate of 2 Hz. Since it is difficult to measure directly the solid-phase temperature of the porous matrix, twelve segments of copper plate of size $60\times6\times2$ mm^3 are fixed on the bottom surface of the foam metal for the measurement of wall temperature (Fig. 2), which represents the solid-phase temperature of the porous matrix at the corresponding axial station. Using high-conductive epoxy at each interface between the aluminum fiber and copper plate minimizes the contact resistance. In addition, the copper segments are spaced by wood strips to minimize axial conduction between them. Twelve copper-constantan thermocouples are distributed along the span-center of each segment, and their junction beads are carefully embedded into the copper segments. In addition, to check the spanwise distribution of the wall temperature, the lateral wall temperature of the first, sixth, and twelfth segments are measured by three thermocouples located at 20 mm away from the span-center of the segment. Results show that the wall temperature difference between the span-center and lateral thermocouples is less than 0.2°C. To ensure that the wall temperature measured above can represent the corresponding solid-phase temperature in the porous matrix, an additional measurement of solid-phase temperature at the real face ($x=L$) of the foam material are conducted by infrared thermography. The infrared camera is focused on the exit plane of the porous medium from the channel outlet to view the solid-phase temperature distribution. Results show that the solid-phase temperature distribution is rather uniform, and the averaged solid-phase temperature compare well with the wall temperature with maximum deviation less than 2°C.

Porous Medium. Figure 3 is a photo showing the structure of aluminum foam (Duocel®, ERG Inc.) investigated, which is manufactured by directional solidification of metal from a superheated liquid state in an environment of overpressure and high vacuum. It has a reticulated structure of open, duodecahedronal-shaped cells connected by continuous, solid metal ligaments. The matrix of cells and ligaments is completely repeatable, regular, and uniform throughout the entirety of the material. The solid ligaments are made of aluminum alloy 6101-T6 that has a thermal conductivity of 218 W/m-K. Table 1 summarizes the properties of the three samples of the aluminum foams that are used in the experimental study. The effective thermal conductivity of the po-

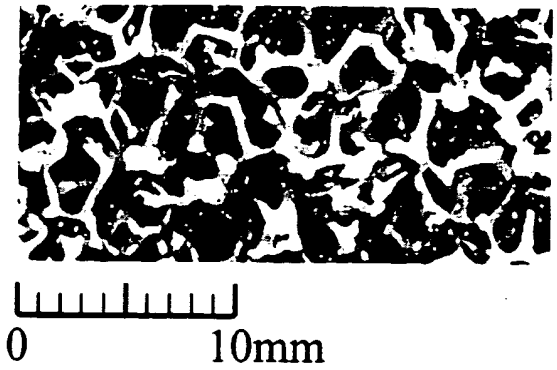

Fig. 3 Photograph of the aluminum foam matrix

rous matrix is expressed by a function of geometry and solid conductivity, i.e., $k_s^* = (1-\varepsilon)k_s$. The volume-based porosity (ε) provided by the manufacturer is determined using the weight of the sample with the density of the aluminum. It is rechecked by determining the void-to-total volume ratio of the sample, in which the sample total volume is measured by its geometry and the pore volume is determined by filling water inside the sample. It should be noted that, due to the manufacturing limitation, the aluminum foam produced by ERG has a small range of porosity about $0.88 \leq \varepsilon \leq 0.97$. In this study, the low-porosity samples of $\varepsilon = 0.7$ and 0.8 are obtained by slowly compressing the aluminum foam of $\varepsilon = 0.95$ (pore density 10 PPI) with identical compression ratio in all directions [19,20]. Measurements of pressure drop/thermal conductivity by rotating the porous matrix relative to flow/temperature gradient direction indicate that the matrix is hydraulically/thermally isotropic. In addition, visual inspections do not reveal any non-uniformity in the structure of matrix. As for the permeability and inertia coefficient of the three aluminum foams, they are determined by the fully developed pressure-drop across the porous sample together with the mean velocity in the porous channel under an isothermal condition. A rearranged version of modified Darcy equation [11] expresses the relationship between these two constants.

$$-\frac{dP}{dx}\cdot\frac{1}{\mu u}=\frac{1}{K}+\frac{F}{\sqrt{K}}\cdot\frac{\rho_f u}{\mu} \tag{1}$$

Figure 4 shows the relationship between $(\Delta P/L)/(\mu u)$ and $\rho_f u/\mu$ for three different porosities investigated. The straight lines are curve-fit results of these measured data with standard deviation less than 11 percent. The permeability K and inertial coefficient F are determined from the intercept together with the slope of the line [11]. According to the estimation method of Antohe et al. [19], the uncertainties of K and F are less than 6 percent and 9 percent, respectively. Note that the length of the present porous matrix should be long enough such that the value of $\Delta P/L$ can well represent the fully developed pressure gradient dP/dx in Eq. (1). To this end, experiments of longer porous matrices of $L = 90$ mm and 120 mm, are conducted to check the entrance and exit effects on the pressure gradient. Results show that in the range of flow velocity investigated the value of $\Delta P/L$ for L = 60 mm is about 5.6 percent and 5.3 percent higher than those of $L = 90$ mm and 120 mm, respectively, which represents the typical entrance and exit effects of the present porous matrix.

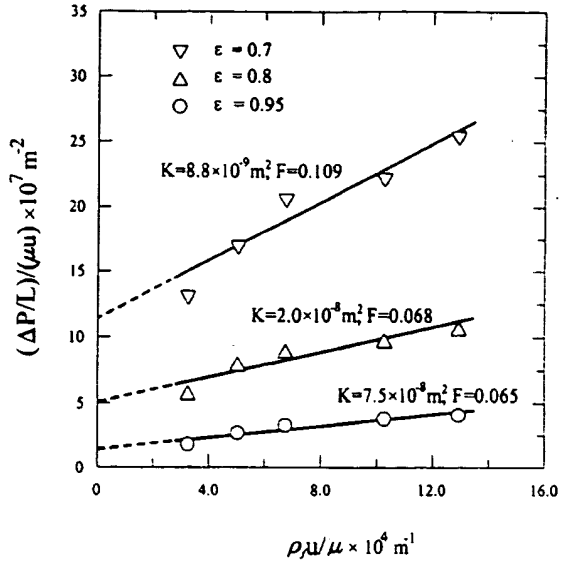

Fig. 4 Relation between $(\Delta P/L)/(\mu u)$ and $\rho_f u/\mu$

Theoretical Simulation

Heat transfer in a porous channel involves a complex thermal transport mechanism between the air and surface of solid matrix. It is difficult to find the exact solutions for the flow and temperature fields. The transient single-blow technique utilized in the present study offers a hot fluid to heat up the porous medium. The physical configuration considered is a rectangular channel filled with the aluminum foam. High temperature airflow passes through and transports energy to the porous medium. The heat transfer characteristic of the porous medium can be evaluated by the transient response of the outlet air temperature, and double rechecked by the wall temperature distribution. To establish a mathematical model, the following assumptions and simplifications are employed.

1 The inlet fluid temperature is uniform. Temperature variations of the solid and fluid in the porous channel depend only on the position along the flow direction and time; therefore, it is a one-dimensional transient problem.
2 The medium is isotropic and has a uniform porosity.
3 The fluid flow is steady and incompressible; its thermal physical properties are constant.
4 There is no local thermal equilibrium between air and solid.
5 The fluid velocity in the porous channel is uniform.

The governing equations are developed by application of the local volume-average technique. This averaging process may obscure local pore phenomena that contribute to the global transport. Energy equations for the solid and fluid phases are as follows:

Table 1 Physical properties of the aluminum foam

Porosity, ε	0.70	0.80	0.95
Average Ligament Diameter, L_d (mm)	0.36	0.36	0.36
Thermal Conductivity, k_s^* (W/m-K)	65.4	43.6	10.9
Mean Cell Size, d (mm)	1.84	1.92	2.03
Permeability, $K \times 10^8$ (m^2)	0.88	2	7.5
Inertial Coefficient, F	0.11	0.068	0.065

Table 2 Coefficients under various flow parameters

ε	Re	ζ_1	ζ_2
0.7	1900	8.2	4.0
	2800	8.8	4.7
	3800	8.1	3.2
	6100	8.8	2.1
	7800	9.5	1.8
0.8	1900	4.7	0.1
	2800	6.0	0.8
	3800	6.5	0.1
	6100	7.7	0.1
	7800	7.6	0.1
0.9	1900	11.1	0.2
	2800	13.9	1.6
	3800	12.1	1.3
	6100	18.2	0.5
	7800	16.0	1.6

$$(1-\varepsilon)(1+\zeta_1)(\rho c_p)_s\frac{\partial T_s}{\partial t}=h_v(T_f-T_s)+k_s^*\left(\frac{\partial^2 T_s}{\partial x^2}\right) \quad (2)$$

$$\varepsilon(\rho c_p)_f\left(\frac{\partial T_f}{\partial t}+\frac{U}{\varepsilon}\frac{\partial T_f}{\partial x}\right)=h_v(T_s-T_f)+(k_f^*+k_t^*)\left(\frac{\partial^2 T_f}{\partial x^2}\right) \quad (3)$$

In Eq. (2) ζ_1 is a constant to modify the time delay due to heat capacity and heat loss of the copper plate on the porous medium. k_f^* and k_s^* are the equivalent conductivity of the solid and fluid phases, respectively, and are represented as εk_f and $(1-\varepsilon)k_s$. Moreover, k_t^* is the transverse thermal dispersion conductivity due the fluctuating tortuous air motion in the solid matrix. According to the simple model reported by Hunt and Tien [11], the dispersion conductivity is expressed as $k_t^*=0.025(\rho c_p)_f\sqrt{K}U$.

The appropriate initial and boundary conditions are

$$T_s(0,x)=T_f(0,x)=T_r \quad (4)$$

$$(1-\varepsilon)k_s\frac{\partial T_s}{\partial x}(t,0)=(1+\zeta_2)h_vL[T_i(t)-T_s(t,0)] \quad (5)$$

$$\frac{\partial T_s}{\partial x}(t,L)=0 \quad (6)$$

$$T_f(t,0)=T_i(t) \quad (7)$$

$$\frac{\partial T_f}{\partial x}(t,L)=0. \quad (8)$$

ζ_2 is another constant to modify the inlet boundary condition due to the heat transfer enhancement by the random structure of the porous medium. These weighting factors could be determined by trial and error via comparing the measured and predicted wall temperature distributions. Table 2 summarizes the values of ζ_1 and ζ_2 selected for different flow and parameters in the present study. T_i is the inlet air temperature and is determined from the measurement. By introducing the following variables:

$$\theta=\frac{T-T_r}{T_{\text{final}}-T_r};\quad X=\frac{x}{L};\quad \tau=\frac{t}{(L/U)};$$

$$C_1=\frac{(\rho c_p)_f}{(\rho c_p)_s(1+\zeta_1)};\quad C_2=\frac{k_s(\rho c_p)_f}{k_f(\rho c_p)_s(1+\zeta_1)};$$

$$\text{St}=\frac{h_vL}{(\rho c_p)_fU};\quad \text{Re}=\frac{\rho_fUL}{\mu};\quad \text{Pr}=\frac{\mu(c_p)_f}{k_f};$$

$$\text{Pr}^*=\frac{\mu(c_p)_f}{(k_f^*+k_t^*)};\quad \text{Bi}=\frac{h_vL^2}{k_s},$$

the governing equations can be nondimensionalized as:

$$\frac{\partial\theta_s}{\partial\tau}=\frac{C_1\text{St}}{1-\varepsilon}(\theta_f-\theta_s)+\frac{C_2}{\text{Pr Re}}\frac{\partial^2\theta_s}{\partial X^2} \quad (9)$$

$$\frac{\partial\theta_f}{\partial\tau}+\frac{1}{\varepsilon}\frac{\partial\theta_f}{\partial X}=\frac{\text{St}}{\varepsilon}(\theta_s-\theta_f)+\frac{1}{\varepsilon\text{Pr}^*\text{ Re}}\frac{\partial^2\theta_f}{\partial X^2}. \quad (10)$$

The dimensionless forms of the initial and boundary conditions are as follows:

$$\theta_s(0,X)=\theta_f(0,X)=0 \quad (11)$$

$$\frac{\partial\theta_s}{\partial X}(\tau,0)+\frac{(1+\zeta_2)\text{Bi}}{1-\varepsilon}[\theta_i-\theta_s(\tau,0)]=0 \quad (12)$$

$$\frac{\partial\theta_s}{\partial X}(\tau,1)=0 \quad (13)$$

$$\theta_f(\tau,0)=\theta_i \quad (14)$$

$$\frac{\partial\theta_f}{\partial X}(\tau,1)=0. \quad (15)$$

Using a guessed value of volumetric heat transfer coefficient (h_v) together with the prescribed values of geometric properties, physical properties, measured inlet air temperatures, a volumetric flow rate, and proper choices of empirical constants of ζ_1 and ζ_2, the solid and fluid phase temperatures, i.e., θ_s and θ_f, can be solved from Eqs. (9) and (10). Then, the value of h_v is modified until the accuracy between predicted and measured exit air temperatures is satisfactory (typically with deviation less than 1.0×10^{-3}). The flowchart of the transient single-blow technique is showed in Fig. 5.

The methodology used to solve the above equations associated with the boundary and initial conditions is based on the control volume, finite-difference technique [21]. The transient finite-difference form of the energy equations is solved explicitly by a line-by-line iterative method. Stepping forward in time and retaining a converged solution at each time step handle the time dependence. The sensitivity studies of node number and time increment are performed to check the stability and accuracy of the numerical scheme. Five sets of node numbers, i.e., 40, 60, 100, 150, and 200, are tested to ensure that the results of the present study are grid independent. A comparison of θ_f between 100 nodes and 150 nodes reveals accuracy up to three significant figures, suggesting that 100 nodes ($\Delta X=0.01$) are sufficient to obtain grid independent results. In addition, the effect of time step on the results is examined by testing several time steps of $\Delta\tau=0.05$, 0.1, 0.2, and 0.5. The results indicate that there is no significant difference be-

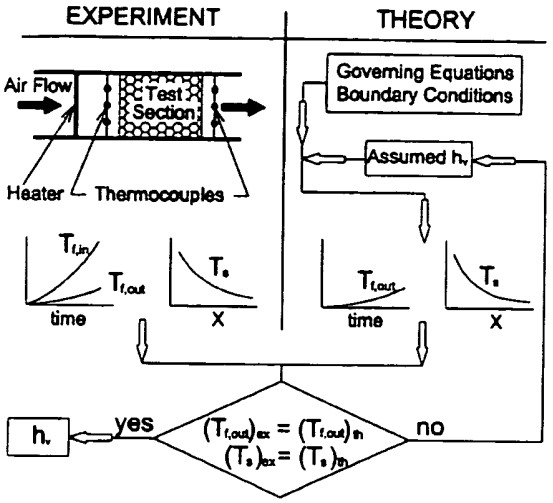

Fig. 5 Flow chart of the transient single-blow technique

tween the results using time increments of 0.05 and 0.1. Hence, the entire calculations are carried out with $\Delta X = 0.01$ and $\Delta \tau = 0.05$.

Data Analysis and Uncertainty

Friction Factors. The friction factor of the present foam channel is calculated from the pressure drop across the test channel and the bulk velocity of the air and expressed as

$$C_f = -2\Delta P/(\rho_f \cdot U^2). \tag{16}$$

Note that based on the heating level of this study, it is experimentally determined that the friction factor with heating is only about 2 percent higher than that without heating. Therefore, for time saving, the friction factor is based on the isothermal conditions without the tedious heating process. The individual uncertainties for ΔP and U are 5.5 percent and 3.0 percent, respectively. The maximum uncertainty of C_f is estimated to be less than 7.3 percent for Reynolds number greater than 1900 by the uncertainty estimation method of Kline and McClintock [22].

Interstitial Heat Transfer Coefficient. The errors of heat transfer coefficient are produced mainly due to the deviation of temperature measurement and the root-mean-square of the difference between the values of experiment and computation. The uncertainty in temperature measurement is about 3.3 percent. The maximum uncertainty in the root-mean-square of the temperature difference is less 14.0 percent. The combination of root-sum-square is employed to calculate the overall uncertainty of the volumetric heat transfer coefficient. As a result, the overall uncertainty of h_v is 14.0 percent.

Results and Discussion

Friction Factor. The effect of the Reynolds number (Re) on the friction factor (C_f) for the flow across the channel inserted with the aluminum foam is shown in Fig. 6. Three aluminum foams of different porosities are tested, i.e., $\varepsilon = 0.7$, 0.8, and 0.95. The data points are the exact experiment and the lines passing through these points are least-square results. It is seen that the friction factor decreases with increasing Reynolds number for all porosities investigated. The aluminum foam of higher porosity has a lower friction factor due to the less channel blockage together with a smaller surface drag. To qualitatively understand the drag of flow across different-porosity foams, a comparison of the flow patterns around different-porosity aluminum foams is shown in Fig. 7, which is measured by a smoke-wire technique [23]. The

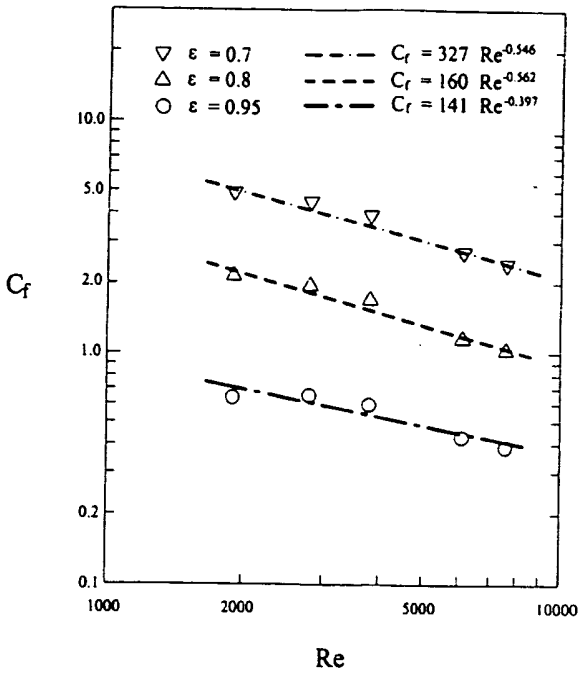

Fig. 6 Friction factor in the aluminum foam channel

smoke wire is placed vertically along the duct center on the axial station ahead of aluminum foam. Instead of the thick-sample (60 mm) employed in the heat transfer experiment, a slender aluminum foam (10 mm) is used herein for easier permeable. The airflow is from left to right. Figure 6(*a*) shows the flow over a smooth plane channel without porous medium and serves as a reference. Figures 6(*b*) and (*c*) are the results of $\varepsilon = 0.7$ and 0.95, respectively. For $\varepsilon = 0.7$, it is seen that some smokes stay in front of the aluminum foam, meaning that the flow cannot easily penetrate the aluminum foam due to a large blockage. In contrast, the flow for $\varepsilon = 0.95$ seems to pass smoothly through the aluminum foam. The above flow-structure comparison has reasonably illustrated the effect of porosity on the friction factor showing in Fig. 6. Another interesting observation by comparing Figs. 7(*b*) and (*c*) is that the flow structures behind the aluminum foam are different. A large amount of eddies is clearly observed behind the rear face of the aluminum foam for $\varepsilon = 0.7$ and, however, the flow after the

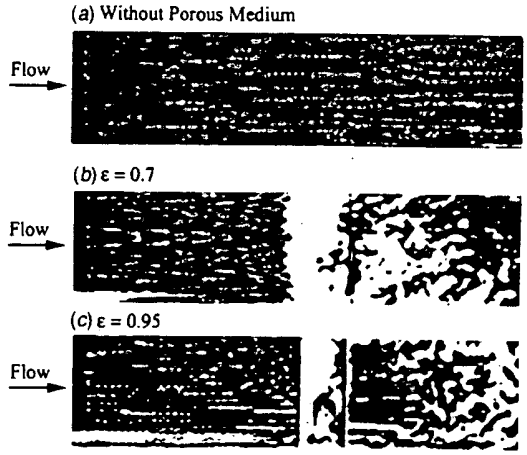

Fig. 7 Comparison of flow structure around the aluminum foams of different porosities

Table 3 Coefficients of friction factor correlations of the porous channel

ε	$C_f = a_1 \mathrm{Re}^{a_2}$			
	a_1	a_2	Deviations	Eq.
0.95	141	-0.397	4.2 %	(17-1)
0.80	160	-0.562	5.5 %	(17-2)
0.70	327	-0.546	3.4 %	(17-3)

high-porosity aluminum foam (ε=0.95) is relatively laminar. Therefore, we may extrapolate this fact to that the flow inside the foam material of ε=0.7 would be more turbulent than that of ε=0.95, which largely affects the heat transfer characteristics inside the porous medium and will be shown later. The data presented in Fig. 5 could be correlated as the following equations:

$$C_f = a_1 \mathrm{Re}^{a_2}, \tag{17}$$

where the coefficients a_1 and a_2 for various foam porosities are listed in Table 3. The maximum deviation between the equation above and the experimental data is only 5.5 percent.

Heat Transfer Characteristics. Typical examples of the histories of inlet and outlet air temperatures during the present experiment for the single-blow technique are shown in Fig. 8 under various ε and Re. The solid circles in each figure are the measured inlet air temperatures, while the solid lines passing through these circles are the curve-fitted results (by the 5th order polynomials) that serve as the inlet condition to the present theoretic model equations. The solid triangles are the measured outlet air temperatures, while the dashed lines are the calculating results from the present theoretic model using the volumetric heat transfer coefficient listed in each figure. In general, the theoretically simulated outlet air temperatures are in good agreement with the experimental ones, indicating the appropriate volumetric heat transfer coefficient selected in each case. It should be noted that in all tests the heat dissipated from the electric heater is controlled to be constant by adjusting the current through the resistance of the heater. Although the range of abscissa (time) displayed in each figure may be different, the histories of the inlet air temperatures under the same mass flow rate (Re) are essentially the same. As shown in Figs. 8(a)–(c) for Re=1900, with the same history of the inlet air temperature, the smaller the foam porosity is, the slower is the incremental rate of the outlet air temperature. For example, at time step of τ=100, the outlet air temperatures are θ_o=0.027, 0.016, and 0.008, respectively, for ε=0.95, 0.08, and 0.7. This means that the aluminum foam of a small porosity has a large heat capacity that reduces the incremental rate of the outlet air temperature. There is a significant heat exchange between the air and solid matrix for the small-porosity aluminum foam. Attention is now turned to the effect of the Reynolds number showed in Fig. 8(c), in which the difference between the inlet and outlet air temperatures is roughly the same for Re=1900 and 6100. It has clearly showed that the higher Reynolds number (Re=6100) requires more time to reach the same temperature difference than the lower Reynolds number (Re=1900). This is because a higher Reynolds number has a higher heat transfer coefficient inside the porous medium that removes more heat from the air to the porous medium, and thus requires more time to increase the difference of the inlet and outlet air temperatures. Figure 9 presents the temperature distribution of the solid material (the aluminum foam) along the streamwise direction. It is found that the theoretic curves agree fairly well with the experimental data. This confirms again the correctness of the predicted heat transfer coefficient.

There is a broad variety of constraints that may be utilized in evaluating the thermal performance of the channel with porous medium [24,25]. In this paper, thermal performance comparisons among the three aluminum-foam channels are made for two sets of constraints that are widely employed, namely, the same through flow rate and the same pumping power. The comparison of heat transfer coefficients for the same airflow rate constraint is made in Fig. 10, which shows the Nusselt number as a function of the Reynolds number for three different aluminum foams. The corresponding volumetric heat transfer coefficient (h_v) is also plotted on the right-hand side of ordinate of this figure. As shown in Fig. 10, the Nusselt number increases with increasing the Reynolds number. For a fixed Reynolds number, the heat transfer coefficient increases with decreasing the porosity due to an increase in local fluid velocity and, partly, the enhancement of turbulent transport inside the foam (Fig. 7). Attention is now turned to the same pumping power constraint. The pumping power required to drive a fixed volumetric flow rate ($\dot{V}$) in the foam duct can be written as $\Delta P \cdot \dot{V}$. As shown in Fig. 6, the pressure drop is higher for the foam channel of a lower porosity. Therefore, the use of low-porosity foam instead of high-porosity foam should reduce the through flow rate to keep the fluid pumping power constant in a porous channel, which lead to a reduction in the heat transfer coefficient. To implement this case, Fig. 11 shows the Nusselt number as a function of the nondimensional pumping power $C_f \cdot \mathrm{Re}^3$. From this figure, it is seen that the volumetric heat transfer coefficient increases with increasing the nondimensional pumping power for all aluminum-foam channels. Further inspection of this figure reveals that the aluminum-foam channel of ε=0.8 has the best thermal performance among the three aluminum-foam channels. This is because the aluminum-foam channel for ε=0.8 is accompanied by a moderate pressure-drop (Fig. 6) and produces a sufficiently high heat transfer, and thus yields the highest thermal performance.

Comparison With Previous Results. A comparison of the present and previous interstitial heat transfer results is made in Fig. 12. The volumetric heat transfer coefficient is expressed in dimensionless form in terms of the pore Nusselt number (Nu_d), which is plotted against the pore Reynolds number (Re_d) in Fig. 12. In general, the mean pore diameter appears to be a reasonable choice for the characteristic length in defining the Nusselt number and Reynolds number in the foam materials [12]. In this figure, the present data are presented by open symbols, and the straight lines passing through these symbols are least-square fits, and can be expressed as

$$\mathrm{Nu}_d = b_1 \mathrm{Re}_d^{b_2}. \tag{18}$$

The coefficients b_1 and b_2 for various porosities and the maximum deviation between the equation above and the experimental data are listed in Table 4. Note that the data of pore Nusselt numbers for ε=0.7 and 0.8 gather closely, and can be further correlated as a single equation with a reasonable deviation. As for the previous interstitial heat transfer results, the data band represents the results obtained from ceramic foams of $0.83 \leqq \varepsilon \leqq 0.87$ by using a single-blow technique [12], which consists of three correlations for various pore diameters d=0.76, 0.94 and 1.52 mm. The Reynolds-number dependence (Re_d^n) for these correlations ranges from n=0.7 to 0.96. In addition, The dashed line is the volumetric heat transfer coefficient inside a ceramic-aluminum foam for ε=0.87, which is obtained by comparing the measured and predicted Nusselt number on the heated wall of a porous channel [13]. A light irregularity of the curve at Re_d=20 is because of the inconsistency of results obtained for d=2.0 and 4.2 mm at the same Reynolds number. Furthermore, the centerline is

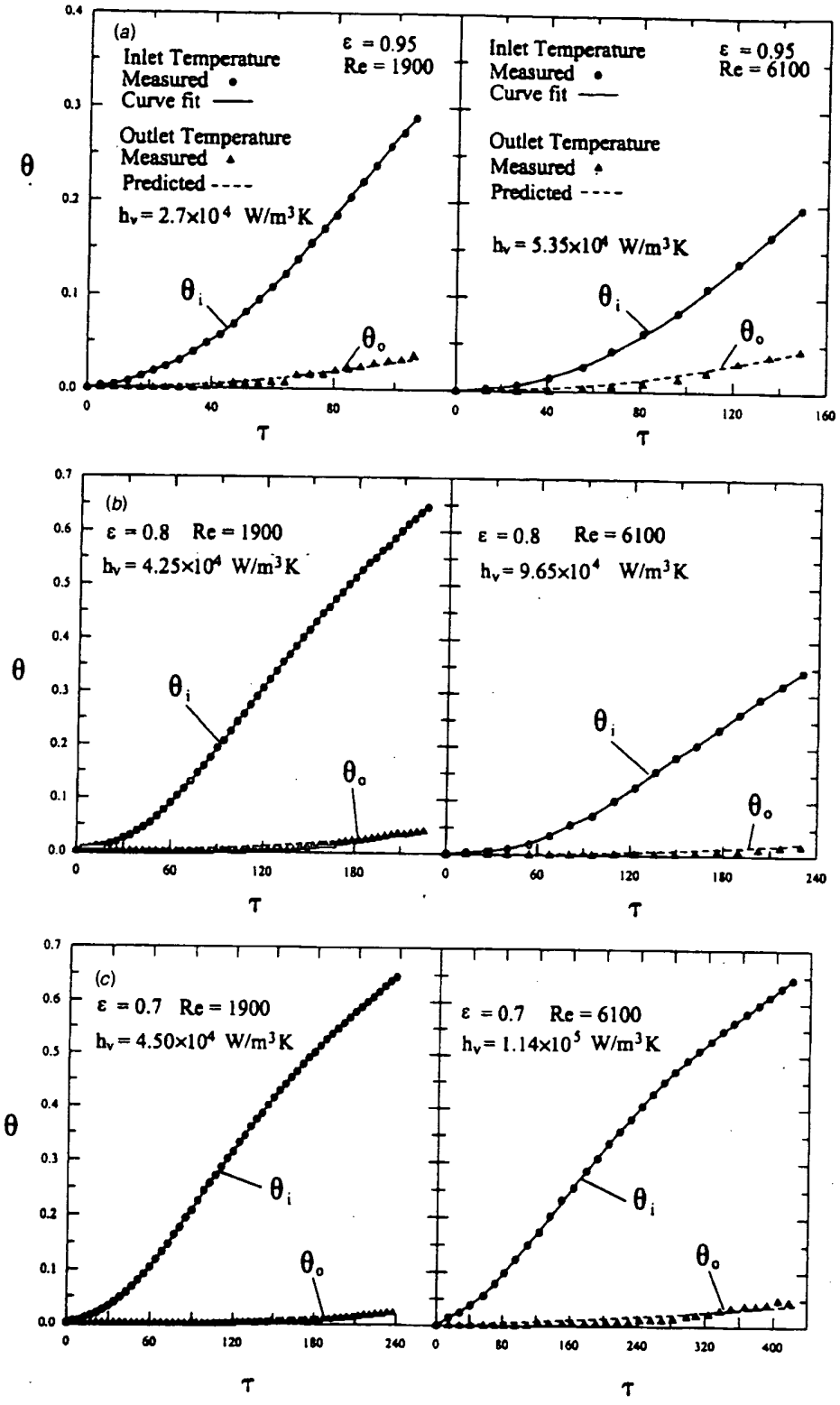

Fig. 8 Histories of the inlet and outlet air temperatures

an empirical correlation compiled from transient and steady state data of packed spherical particles. This correlation is unique and covers a broad range of porosity and Reynolds number [25].

It is seen from this figure that the Reynolds-number dependence (Re_d^n) of the present data ($n = 0.6–0.83$) is largely similar to that of Younis and Viskanta [12]. Quantitatively, the present data for $\varepsilon = 0.7$ and 0.8 can extrapolate well to those in low pore Reynolds numbers obtained by Ichimiya [13] but are slightly lower than those of Younis and Viskanta [12]. This discrepancy in heat transfer coefficient may be attributed to the different size (in stream-

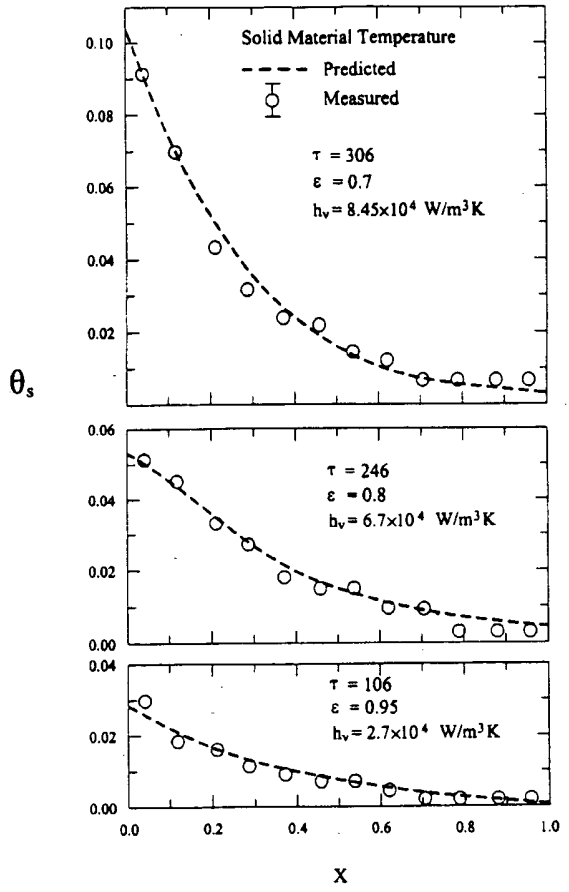

Fig. 9 Solid material temperature distributions along the streamwise direction

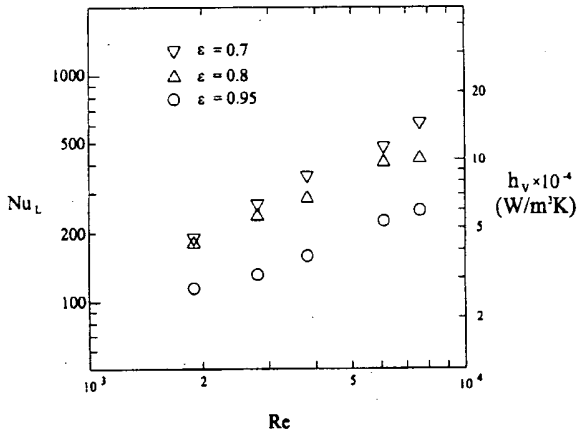

Fig. 10 Volumetric heat transfer coefficient as a function of the Reynolds number

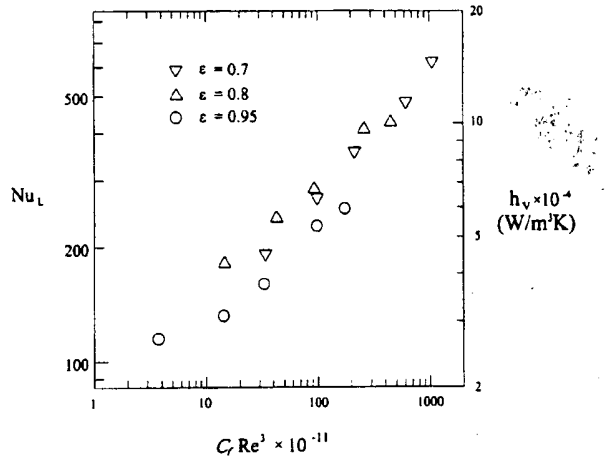

Fig. 11 Volumetric heat transfer coefficient as a function of the nondimensional pumping power

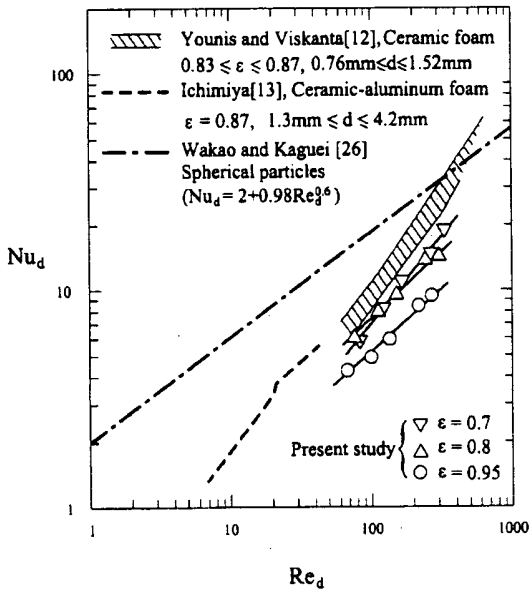

Fig. 12 Comparison of the pore Nusselt number between the present and previous works

wise direction) of foam used between Younis and Viskanta [12] and the present work. In Younis and Viskanta [12], a shorter ceramic porous medium (12–14 mm) than the present one (60 mm) will cause a more significant entrance effect that increases the length-mean heat transfer coefficient. Nevertheless, the above comparison between the present data with those by Younis and Viskanta [12] and Ichimiya [13] is satisfactorily in agreement. It is further seen that the correlation proposed by Wakas and Kaguei [26] seems to be invalid for the data presented, especially in the

Table 4 Coefficients of heat transfer correlations

ε	$Nu_d = b_1 Re_d^{b_2}$			
	b_1	b_2	Deviation	Eq.
0.95	0.3248	0.601	1.5 %	(18-1)
0.80	0.3760	0.644	1.0 %	(18-2)
0.70	0.1569	0.825	0.6 %	(18-3)
0.70 + 0.80	0.2396	0.737	2.4 %	(18-4)

low Reynolds number range. We attribute this to the fact that the porous structures of the present foam material are different from those of the packed beds, which has a large influence on the convective heat transfer through affecting the shape of the flow passages as well as the surface area per unit volume.

Conclusions

Interstitial heat transfer and friction characteristics for flow across a channel inserted with aluminum foams have been studied experimentally. The combined effects of foam porosity ($\varepsilon=0.70$, 0.80, and 0.95) and flow Reynolds number ($1900 \leqq Re \leqq 7900$) are examined in detail. A transient single-blow technique has been applied to the determination of the interstitial heat transfer coefficient of the aluminum foam. The results of numerical simulation coincide with those of experimental measurement by using the thermal non-equilibrium energy equations together with appropriate thermal boundary conditions and proper choices of the empirical constants ζ_1 and ζ_2. Main findings based on the data presented are as follows.

1 At a fixed Reynolds number, as the porosity of the aluminum foam increases from $\varepsilon=0.70$ to 0.95, the friction factor decreases due to the decrease in the channel blockage. The friction factor decreases with an increase of Reynolds number for all porosities investigated.

2 Under the same through flow rate and history of the inlet air temperature, the small-porosity aluminum foam has a slow incremental rate of the outlet air temperatures, meaning that the aluminum foam of a small porosity has a large heat capacity.

3 At a fixed Reynolds number, the volumetric heat transfer coefficient inside the aluminum foam increases with decreasing the porosity due to the increase in local fluid velocity and the enhancement of turbulence transport. In addition, the volumetric heat transfer coefficient increases with increasing the Reynolds number under a fixed value of foam porosity.

4 Among the three aluminum foams investigated, the foam channel of $\varepsilon=0.8$ appears the best thermal performance under constant pumping power constraint because it produces a satisfactorily high heat transfer and is accompanied by a moderate pressure drop.

5 Empirical correlations of pore Nusselt number for three aluminum foams under a specific length ($L=60$ mm) are developed in terms of pore Reynolds number for the first time, which can be helpful in the design of the related devices such as compact heat exchangers or thermal energy absorbers. Further efforts are required to conclude a unique correlation that covers a wide range of the flow and geometric parameters such as the porosity of foam metal, Reynolds number, etc.

Acknowledgments

This work was sponsored by the National Science Council of the Republic of China under contract No. NSC 85-2212-E-216-003.

Nomenclature

Bi = Biot number, $h_v L^2/k_s$
C_1 = constant $C_1=(\rho c_p)_f/[(\rho c_p)_s(1+\zeta_1)]$;
C_2 = constant $C_2=k_s(\rho c_p)_f/[k_f(\rho c_p)_s(1+\zeta_1)]$
C_f = friction factor, Eq. 16
c_p = isobaric specific heat, kJ/kg-K
d = mean pore diameter, m
F = inertia coefficient constant
h_v = volumetric heat transfer coefficient, W/m^3-K
K = permeability, m^2
k = thermal conductivity, W/m-K
L = test section length, m
Nu = Nusselt number based on porous matrix length, $h_v L^2/k_f$
Nu_d = pore Nusselt number, $h_v d^2/k_f$
P = pressure, N/m^2
Pr = Prandtl number $(\mu c_p)_f/k_f$
Re = Reynolds number, $\rho_f U L/\mu$
Re_d = pore Reynolds number, $\rho_f U d/(\varepsilon\mu)$
St = Stanton number, $h_v L/[(\rho c_p)_f U]$
T = temperature, K
T_{final} = steady state fluid temperature at test section inlet, K
T_r = reference (room) temperature, K
t = time, s
U = mean velocity in the rectangular channel, m/s
u = pore velocity, m/s
X = dimensionless axial length, x/L
x = axial length, m
ε = porosity
θ = dimensionless temperature $(T-T_r)/(T_{final}-T_r)$
μ = viscosity, kg/m-s
ρ = density, kg/m^3
τ = dimensionless time, $U\cdot t/L$
ζ_1, ζ_2 = constants

Subscripts

d = pore
f = fluid
i = inlet value
s = solid

Superscripts

$*$ = equivalent value

References

[1] Koh, J. C. Y., and Stevens, R. L., 1975, "Enhancement of Cooling Effectiveness by Porous Medium in Coolant Passages," ASME J. Heat Transfer, **96**, pp. 309–311.
[2] Cheng, P., 1982, "Mixed Convection About a Horizontal Cylinder and a Sphere in Fluid Saturated Porous Medium," Int. J. Heat Mass Transf., **28**, pp. 1245–1247.
[3] Jones, D. P., and Krier, H., 1983, "Gas Flow Resistance Measurements Through Packed Beds at High Reynolds Number," ASME J. Fluids Eng., **105**, pp. 168–173.
[4] Cheng, P., and Zhu, H., 1987, "Effects of Radial Thermal Dispersion on Fully Developed Forced Convection in Cylindrical Packed Bed," Int. J. Heat Mass Transf., **30**, pp. 2373–2383.
[5] Renken, K. J., and Poulikakos, D., 1988, "Experimental and Analysis of Forced Convection Heat Transport in Packed Bed of Spheres," Int. J. Heat Mass Transf., **31**, pp. 1399–1408.
[6] Vafai, K., and Sozen, M., 1990, "Analysis of Energy and Momentum Transport for Fluid Flow through a Porous Bed," ASME J. Heat Transfer, **112**, pp. 690–699.
[7] Amiri, A., and Vafai, K., 1994, "Analysis of Dispersion Effect and Nonthermal Equilibrium, Non-Darcy Variable Porosity Incompressible Flow Through Porous Media," Int. J. Heat Mass Transf., **37**, pp. 939–954.
[8] Hwang, G. J., and Chao, C. H., 1994, "Heat Transfer Measurement and Analysis for Sintered Porous Channel," ASME J. Heat Transfer, **116**, pp. 456–464.
[9] Varahasamy, M., and Fand, R. M., 1996, "Heat Transfer by Forced Convection in Pipes Packed with Porous Media Whose Matrices Are Composed of Spheres," Int. J. Heat Mass Transf., **39**, pp. 3931–3947.
[10] Peterson, G. P., and Chang, S. W., 1998, "Two-Phase Heat Dissipation Utilizing Porous-Channels of High Conductivity Material," ASME J. Heat Transfer, **120**, pp. 243–252.
[11] Hunt, M. L., and Tien, C. L., 1988, "Effects of Thermal Dispersion on Forced Convection in Fibrous Media," Int. J. Heat Mass Transf., **31**, pp. 301–309.
[12] Younis, L. B., and Viskanta, R., 1993, "Experimental Determination of the Volumetric Heat Transfer Coefficient Between Stream of Air and Ceramic Foam," Int. J. Heat Mass Transf., **36**, pp. 1425–1434.
[13] Ichimiya, K., 1999, "A New Method for Evaluation of Heat Transfer Between Solid Material and Fluid in a Porous Medium," ASME J. Heat Transfer, **121**, pp. 978–983.
[14] Calmidi, V. V., and Mahajan, R. L., 2000, "Forced Convection in High Porosity Metal Foams," ASME J. Heat Transfer, **122**, pp. 557–565.
[15] Genetti, A. J., 1999, "Engineering and Design—Groundwater Hydrology," *USACE*, Washington DC.
[16] Hadim, A., 1994, "Forced Convection in a Porous Channel with Localized Heat Sources," ASME J. Heat Transfer, **116**, pp. 465–472.
[17] Golombok, M., Jariwala, H., and Shirvill, L. C., 1990, "Gas-Solid Heat Exchange in a Fibrous Metallic Material Measured by a Heat Regenerator Technique," Int. J. Heat Mass Transf., **33**, pp. 243–252.
[18] Gamson, B. W., Thodos, G., and Hougen, O. A., 1943, "Heat, Mass and

Momentum Transfer in the Flow of Gases Through Granular Solids," AIChE J., **39**, pp. 1–35.
[19] Antohe, B. V., Lage, J. L., Price, D. C., and Weber, R. M., 1997, "Experimental Determination of Permeability and Inertia Coefficients of Mechanically Compressed Aluminum Porous Matrices," ASME J. Fluids Eng., **119**, pp. 404–412.
[20] Lage, J. L., Antohe, B. V., and Nield, D. A., 1997, "Two Type of Nonlinear Pressure-Drop Versus Flow Rate Relation Observed For Saturated Porous Media," ASME J. Fluids Eng., **119**, pp. 700–706.
[21] Patankar, S. V., 1980, *Numerical Heat Transfer and Fluid Flow*, Hemisphere, New York.
[22] Kline, S. J., and McClintock, F. A., 1953, "Describing the Uncertainties in Single-Sample Experiments," Mech. Eng. (Am. Soc. Mech. Eng.), pp. 3–8.
[23] Hwang, J. J., 1998, "Heat Transfer-Friction Characteristic Comparison in Rectangular Ducts With Slit and Solid Ribs Mounted on One Wall," ASME J. Heat Transfer, **120**, pp. 709–716.
[24] Hwang, J. J., 1997, "Turbulent Heat Transfer and Fluid Flow in a Porous-Baffled Channel," J. Thermophys. Heat Transfer, **11**, pp. 429–436.
[25] Hwang, J. J., and Chao, C. H., 2000, "Passive Control of Convective Transport Phenomena Utilizing an Attached-Detached Rib-Array," J. Thermophys. Heat Transfer, **14**, pp. 579–583.
[26] Wakao, N., and Kaguei, S., 1993, *Heat and Mass Transfer in Packed Beds*, Gordon and Breach Science.